
Research Article: Methods/New Tools | Novel Tools and Methods

Automatic Cell Segmentation by Adaptive Thresholding (ACSAT) for large scale calcium imaging datasets

Simon P. Shen¹, Hua-an Tseng², Kyle R. Hansen², Ruofan Wu³, Howard Gritton², Jennie Si³ and Xue Han²

¹*Department of Physics, Harvard University, Cambridge, MA 02138, USA*

²*Biomedical Engineering Department, Boston University, Boston, MA 02215, USA*

³*School of Electrical, Computer and Energy Engineering, Tempe, AZ 85287, USA*

DOI: 10.1523/ENEURO.0056-18.2018

Received: 3 February 2018

Revised: 16 August 2018

Accepted: 23 August 2018

Published: 4 September 2018

Author Contributions: S.P.S. designed research, performed research, contributed unpublished reagents/analytic tools, analyzed data, and wrote the paper; H.T. performed research, analyzed data, and wrote the paper; K.R.H. performed research; R.W. analyzed data; H.G. performed research; J.S. and X.H. designed research and wrote the paper.

Funding: NIH Director's new innovator award
1DP2NS082126

Funding: Pew Foundation

Funding: DARPA Young Faculty Award

Funding: Boston University Biomedical Engineering Department

Funding: National Science Foundation Graduate Research Fellowship
DGE-1247312

Conflict of Interest: Authors report no conflict of interest.

X.H. acknowledges funding from NIH Director's new innovator award (1DP2NS082126), Pew Foundation, DARPA Young Faculty Award, Boston University Biomedical Engineering Department. K.R.H. is supported by a National Science Foundation Graduate Research Fellowship under Grant No. DGE-1247312.

S.P.S. and H.T. are co-first authors

In the "Materials and Methods: Mouse preparation" section, "All animal procedures were approved by [Author University = Boston University] Institutional Animal Care and Use Committee."

In the "Materials and Methods: Code accessibility" section, "The code/software described in the paper is freely available online at [redacted for double-blind review = www.github.com/sshen8/acsat]."

Correspondence address: Jennie Si, Tel.: 480-965-6133; E-mail: si@asu.edu; Xue Han, Tel.: 617-358-6189; E-mail: xuehan@bu.edu

Cite as: eNeuro 2018; 10.1523/ENEURO.0056-18.2018

Alerts: Sign up at eneuro.org/alerts to receive customized email alerts when the fully formatted version of this article is published.

Accepted manuscripts are peer-reviewed but have not been through the copyediting, formatting, or proofreading process.

Copyright © 2018 Shen et al.

This is an open-access article distributed under the terms of the Creative Commons Attribution 4.0 International license, which permits unrestricted use, distribution and reproduction in any medium provided that the original work is properly attributed.

1 Automatic Cell Segmentation by Adaptive Thresholding (ACSAT) for large scale calcium imaging datasets

2

3 Running Title: Auto Cell Segmentation by Adaptive Thresholding

4

5 Simon P. Shen^{1*}, Hua-an Tseng^{2*}, Kyle R. Hansen², Ruofan Wu³, Howard Gritton², Jennie Si^{3**}, Xue Han^{2**}

6 ¹ Department of Physics, Harvard University, Cambridge, MA 02138

7 ² Biomedical Engineering Department, Boston University, Boston, MA 02215

8 ³ School of Electrical, Computer and Energy Engineering, Tempe, AZ 85287

9 *S.P.S. and H.T. are co-first authors

10

11 Contributions:

12 S.P.S. designed research, performed research, contributed unpublished reagents/analytic tools, analyzed
13 data, and wrote the paper; H.T. performed research, analyzed data, and wrote the paper; K.R.H.
14 performed research; R.W. analyzed data; H.G. performed research; J.S. and X.H. designed research and
15 wrote the paper.

16

17 ** X.H. and J.S. are co-correspondence

18 J.S.: 480-965-6133; si@asu.edu

19 X.H.: 617-358-6189; xuehan@bu.edu

20

21 Number of Figures: 11

22 Number of Tables: 0

23 Number of Multimedia: 2

24 Number of words for Abstract: 209

25 Number of words for Significance Statement: 118

26 Number of words for Introduction: 749

27 Number of words for Discussion: 1713

28

29 Authors report no conflict of interest

30

31 X.H. acknowledges funding from NIH Director's new innovator award (1DP2NS082126), Pew Foundation,
32 DARPA Young Faculty Award, Boston University Biomedical Engineering Department. K.R.H. is supported
33 by a National Science Foundation Graduate Research Fellowship under Grant No. DGE-1247312.

34

35 In the "Materials and Methods: Mouse preparation" section, "All animal procedures were approved by
36 [Author University = Boston University] Institutional Animal Care and Use Committee."

37

38 In the "Materials and Methods: Code accessibility" section, "The code/software described in the paper is
39 freely available online at [redacted for double-blind review = www.github.com/sshen8/acsat]."

40 **Automatic Cell Segmentation by Adaptive Thresholding (ACSAT) for large scale**
41 **calcium imaging datasets**

42 **Abstract**

43 Advances in calcium imaging have made it possible to record from an increasingly
44 larger number of neurons simultaneously. Neuroscientists can now routinely image
45 hundreds to thousands of individual neurons. An emerging technical challenge that
46 parallels the advancement in imaging a large number of individual neurons is the
47 processing of correspondingly larger datasets. One important step is the identification of
48 individual neurons. Traditional methods rely mainly on manual or semi-manual
49 inspection, which cannot be scaled for processing large datasets. To address this
50 challenge, we focused on developing an automated segmentation method, which we
51 refer to as Automated Cell Segmentation by Adaptive Thresholding (ACSAT). ACSAT
52 works with a time-collapsed image and includes an iterative procedure that
53 automatically calculates global and local threshold values during successive iterations
54 based on the distribution of image pixel intensities. Thus, the algorithm is capable of
55 handling variations in morphological details and in fluorescence intensities in different
56 calcium imaging datasets. Within this manuscript we demonstrate the utility of ACSAT
57 by testing it on 500 simulated datasets, two wide-field hippocampus datasets, a wide-
58 field striatum dataset, a wide-field cell culture dataset, and a two-photon hippocampus
59 dataset. For the simulated datasets with truth, ACSAT achieved over 80% recall and
60 precision when the signal-to-noise ratio was no less than ~24 dB.

61 **Significance**

62 ACSAT aims at automatically segmenting cells in large-scale calcium imaging datasets.
63 It is based on adaptive thresholding at both global and local levels and iteratively

64 identifies individual neurons in a time-collapsed image. It is designed to address a
65 variety of datasets, potentially involving variations in cell morphology and fluorescence
66 intensity between different datasets. We demonstrate the effectiveness of ACSAT by
67 testing it under a variety of conditions. For the simulated datasets with truth, ACSAT
68 achieved recall and precision rates over 80% when the signal-to-noise ratio was no less
69 than ~24 dB. For the datasets from mouse hippocampus and striatum, ACSAT captured
70 ~80% of human-identified ROIs and even detected some low-intensity neurons that
71 were initially undetected by human referees.

72 **Introduction**

73 The ability to record from a large population of single neurons during behavior greatly
74 facilitates the investigation of the contribution of individual neurons to neuronal network
75 dynamics. Extracellular single-unit recording has traditionally been a method of choice
76 in neurophysiological analyses of single neurons in the brain. Recent improvements,
77 such as the new generation of genetically-encoded calcium sensors GCaMP6 (Chen et
78 al., 2013, Sun et al., 2013), have made it possible to observe hundreds to thousands of
79 individual neurons simultaneously (Ohki et al., 2005, Andermann et al., 2010, Huber et
80 al., 2012, Ziv et al., 2013, Issa et al., 2014, Mohammed et al., 2016). Though indirect,
81 these calcium indicators have been sensitive enough to monitor neuronal activity with
82 high spatiotemporal precision in behaving animals, allowing researchers to examine the
83 activity of populations of a specific cell type (Hofer et al., 2011, Wachowiak et al., 2013,
84 Pinto and Dan, 2015, Allen et al., 2017) or the same cell over an extended period of
85 time (Poort et al., 2015).

86 As the performance of genetically-encoded calcium indicators improved, wide-field
87 microscopy has become feasible for recording the activity of a large population of
88 neurons over an extended anatomical area (Lutcke et al., 2013, Wilt et al., 2013).
89 Although lacking the spatial subcellular resolution of a multiphoton microscope, wide-
90 field microscopes can operate at a higher speed, allowing the simultaneous recording of
91 increasingly larger populations (Ghosh et al., 2011, Ziv et al., 2013, Kim et al., 2016,
92 Mohammed et al., 2016). Advanced microfabrication techniques further miniaturized the
93 wide-field microscope to a microendoscope capable of monitoring neural activity in
94 freely-moving animals (Ghosh et al., 2011, Ziv et al., 2013).

95 An emerging technical challenge that parallels advances in calcium imaging is the
96 processing of large datasets (Hamel et al., 2015). During data analysis, an important
97 step is to identify regions of interest (ROIs) corresponding to individual neurons. As data
98 grows rapidly both spatially and temporally, the traditional labor-intensive approach of
99 manual inspection has to be automated. Principal component analysis (PCA) and
100 independent component analysis (ICA) methods are natural and frequently-used
101 candidates for automating ROI identification (Mukamel et al., 2009). However, if its
102 assumption of statistical independence between neurons is violated, which is often the
103 case in real neural recordings, then the method relies on user selection of parameters
104 for spatial segmentation.

105 Threshold-based methods represent a promising and intuitive alternative for automatic
106 ROI identification. However, several challenges need to be overcome, including
107 variability in recording conditions or fluorescence signal strength across structures,

108 recording subjects, and the imaging field. For example, one of the most referenced
109 thresholding methods, Otsu's method, which automatically selects the optimal threshold
110 value that minimizes the intra-class variance among ROI pixels and among background
111 pixels, would only successfully segment some of the highest-intensity ROIs (Otsu, 1979,
112 Sezgin and Sankur, 2004). Additionally, the multi-class Otsu's method is limited
113 because uneven lighting may result in separate background classes. A waterfall-
114 thresholding approach addresses uneven lighting by iterative thresholding to capture all
115 intensity peaks, but its selection of a threshold value is "*ad hoc*," making it dataset-
116 dependent and user-dependent (Mellen and Tuong, 2009). A feedback loop-based
117 approach for segmenting bacteria cells optimizes the threshold value from the
118 distribution of pixel intensities, but its assumption that the total ROI area remains
119 constant over time does not hold for calcium-imaging datasets because neurons change
120 in brightness (Shen et al., 2015). A recent machine learning-based algorithm uses
121 image gradients and pixel traces to optimize the threshold value, but it still requires a
122 user's subjective input in selecting a background removal factor based on each dataset
123 (Fantuzzo et al., 2017). Other approaches based on edge detection have trouble due to
124 weak fluorescence signal strength in comparison with the background pixels
125 (Sadeghian et al., 2009). Generally, most segmentation methods require a high level of
126 tuning to each individual dataset.

127 To overcome these challenges of diverse imaging datasets, we introduce a new
128 Automated Cell Segmentation by Adaptive Thresholding (ACSAT) algorithm. ACSAT
129 dynamically and automatically determines global and local threshold values based on
130 the distribution of pixel intensities within a time-collapsed image of a recorded image

131 sequence. We demonstrate the utility of ACSAT on simulated datasets, cell culture
132 datasets, and in vivo wide-field and two-photon datasets. For the simulated datasets
133 with truth, ACSAT achieved recall and precision >80% when the signal-to-noise ratio
134 was no less than ~24 dB. ACSAT also captured ~80% of human-identified ROIs in
135 datasets from mouse hippocampus and striatum and was even able to detect low-
136 intensity neurons that were initially undetected by human referees.

137 **Materials and Methods**

138 Wide-field hippocampus and striatum datasets

139 All animal procedures were approved by [Author University – redacted for double-blind
140 review] Institutional Animal Care and Use Committee. Female C57BL/6 mice (8-12
141 weeks old, Taconic, Hudson, NY) were first injected with 250nL AAV9-Syn-
142 GCaMP6.WPRE.SV40 virus (titer: ~6e12 GC/ml, University of Pennsylvania Vector
143 Core). AAV was delivered either into the dorsal CA1 (AP: -2, ML: 1.4, DV: -1.6), or into
144 the dorsal striatum (AP: 0.5, ML: 1.8, DV: -1.6) regions. Injections were performed with
145 a 10 μ L syringe (World Precision Instruments, Sarasota, FL) coupled with a 33 gauge
146 needle (NF33BL, World Precision Instruments, Sarasota, FL) at a speed of 40 nL/min,
147 controlled by a microsyringe pump (UltraMicroPump 3-4, World Precision Instruments,
148 Sarasota, FL). Upon complete recovery, a custom imaging chamber with glass coverslip
149 was surgically implanted on top of the viral injection site by removing the overlying
150 cortical tissue. The imaging chamber was assembled by fitting a circular coverslip (size
151 0; OD: 3 mm) to a stainless steel cannula (OD: 0.317 mm, ID: 0.236 mm) using a UV-
152 curable optical adhesive (Norland Products). During surgery, a custom aluminum

153 headplate was also attached to the skull, which allows head-fixation during the imaging
154 session.

155 Imaging data were acquired with a custom wide-field microscope coupled with a
156 scientific CMOS camera (ORCA-Flash 4.0, C11440-42U, Hamamatsu, Boston MA),
157 controlled by the commercial software package HCImageLive (Hamamatsu, Boston
158 MA). The wide-field microscope consisted of a Leica N Plan 10×0.25 PH1 objective
159 lens, an excitation filter (HQ 470/50), a dichroic mirror (FF506-Di02), an emission filter
160 (FF01-536/40), a commercial SLR lens as the tube lens (Nikon Zoom-NIKKOR 80–200
161 mm f/4 AI-s), and a 5W LED (LZ1-00B200, 460 nm; LedEngin, San Jose CA). Data
162 acquisition was performed at 20 Hz, at a resolution of 1024 x 1024 pixels, with 16-bits
163 per pixel, for about 10-20 minutes. With 10x objective lens, the microscope provided a
164 field of view of 1.343 x 1.343 mm² (1.312 x 1.312 μm²/pixel) of brain tissue. Imaging
165 data was streamed from the camera to RAM of a custom computer (dual Intel Xeon
166 processors, 128 GB RAM, and a GeForce GTX Titan video card) to ensure temporal
167 precision. After each imaging session, data was moved from RAM to hard drive and
168 saved in multi-page tagged image file format.

169 Two hippocampus datasets (A and B) were collected from two mice (dataset A was
170 previously reported by Mohammed et al. (Mohammed et al., 2016)). The mice were
171 trained to perform a trace conditioning task known to involve hippocampal neural activity
172 (Solomon et al., 1986, Moyer et al., 1990, Tseng et al., 2004, Sakamoto et al., 2005). In
173 this task, the animal was trained to associate a conditioned stimulus (a 350 ms long
174 tone) with an unconditioned stimulus (a gentle 100ms air puff to one eye). There was a

175 250 ms trace interval between two stimuli. During each recording session, the animal
176 was head-fixed and performed 40 trials with a randomized 31-36 second inter-trial
177 interval. The hippocampus datasets (1024 x 1024 pixels/frame, 2047 frames, ~100
178 seconds, ~4 GB size) analyzed in this study were part of larger recording sessions
179 (~50GB size).

180 The striatum dataset was collected from a head-fixed animal running on a spherical
181 treadmill system. The treadmill system consisted a styrofoam ball floated by air
182 pressure in a 3D-printed bowl designed as described in (Dombeck et al., 2007) that
183 allowed the animal to move its limbs freely while head-fixed. The mouse was first
184 handled for several days before being head-fixed to the spherical treadmill. Habituation
185 to running on the spherical treadmill while head-fixed occurred over 3-4 days/week at
186 the same time of day as subsequent recording sessions (8-12 hours after lights-on), for
187 several weeks. Single imaging sessions took approximately 25 minutes. Sampling
188 occurred at approximately 20Hz and exposure time was fixed at 20ms. The striatum
189 dataset (~100 seconds, ~4 GB size) contains 2047 frames with 1024 x 1024 pixels per
190 frame and was also part of a larger dataset (~25GB size).

191 Two human referees manually identified ROIs in the hippocampus dataset A and in the
192 striatum dataset to create a set of human-generated ROIs for comparison with ACSAT's
193 segmentation results. This manual selection was done by viewing the image sequence
194 and segmenting ROIs that had fluorescence traces compatible with neuronal dynamics
195 and/or by selecting ROIs from a composite image created from the video sequence and
196 confirming fluorescence traces were compatible with neuronal dynamics.

197 Wide-field cell culture dataset

198 The primary neuron cell dataset was collected from a 10-day-old neuron culture,
199 infected with AAV9-Syn-GCaMP6.WPRE.SV40 virus. Seven days after infection,
200 neurons were imaged at 20 Hz for 60 seconds. The primary neuron culture dataset
201 contains 1201 frames, 1024 x 1024 pixels per frame, recorded with the same imaging
202 setup as for the hippocampus and striatum datasets described above.

203 Two-photon dataset

204 The two-photon dataset was downloaded from the Neurofinder website
205 (<http://neurofinder.codeneuro.org/>, 03.00). GCaMP6f was used as the indicator. The
206 dataset contains 2250 frames with 498 x 490 pixels per frame with resolution 0.588 x
207 0.588 $\mu\text{m}^2/\text{pixel}$.

208 Signal-to-noise ratio (SNR) calculation

209 We calculated the signal-to-noise ratio (SNR) in decibels (dB) as

$$\text{SNR} = 20 \times \log \frac{\mu_{\text{ROI}}}{\sigma_{\text{background}}}$$

210 For the simulated datasets, μ_{ROI} is the mean intensity value of all pixels belonging to all
211 ROIs in the time-collapsed image I_0 , and similarly, $\sigma_{\text{background}}$ is the standard deviation of
212 background pixel intensity values i.e. all pixels that do not belong to an ROI. For the
213 hippocampus dataset A and the striatum dataset, μ_{ROI} is the maximum intensity value of
214 an ROI trace, and $\sigma_{\text{background}}$ is the standard deviation of the background trace. The ROI
215 trace value at each timepoint is the averaged intensity values of all pixels belonging to
216 that ROI, and similarly for the background trace, which uses all pixels not belonging to

217 any ROI. Note that the SNR for the simulated datasets describes the whole time-
218 collapsed image I_0 , whereas the SNR for the hippocampus and striatum datasets
219 describe an individual ROI.

220 Simulated datasets

221 We tested ACSAT's segmentation performance on 500 simulated datasets with varying
222 signal-to-noise ratios (between ~ 19 dB and ~ 29 dB) and numbers of ROIs (between 300
223 and 700). Figure 2B shows some examples of the simulated time-collapsed image, i.e.,
224 the input image I_0 to ACSAT in Figure 1A. The simulation gives us the true locations of
225 all ROIs so that we can accurately assess ACSAT's segmentation performance.

226 Our simulated datasets were obtained by a procedure adapted from (Zhou et al., 2018).
227 We used the model $I_0 = E + AC$ to generate the simulated datasets where E represents
228 noise, A represents the shapes of each ROI, and C adjusts each ROI's intensity to
229 simulate uneven lighting.

230 The pixel noise values in E were randomly sampled from the background pixel values in
231 the time-collapsed image for the hippocampus dataset. This noise is unlikely to be
232 Gaussian because the time-collapsing procedure subtracts the mean value from the
233 maximum value of each pixel such that the time-collapsed image is biased towards
234 higher pixel values.

235 The centroid location of each ROI represented in A was randomly selected with weights
236 C^2 . The pixel values comprising the body of each ROI was modeled deterministically by

237 the bivariate Gaussian probability density function, with widths randomly selected
238 according to Zhou et al. (Zhou et al., 2018).

239 The image C is also used to amplify each ROI's pixel values to reflect uneven lighting
240 conditions across the imaging field. C was generated by applying heavy Gaussian
241 filtering to the time-collapsed image of the hippocampus dataset until no individual ROIs
242 are detectable.

243 Automated Cell Segmentation by Adaptive Thresholding (ACSAT) Overview

244 Fluorescence imaging data obtained in the form of image sequences is processed
245 offline using a custom MATLAB algorithm. Image sequences were first motion-corrected
246 as described in Mohammed et al. (2016) to remove micromotion of the imaged area
247 caused by breathing and other movements of the animal. ACSAT (Figure 1A) is then
248 applied to a time-collapsed image that represents the image sequences, to
249 automatically identify individual neurons as regions of interest (ROIs).

250 The input image sequence is first loaded into MATLAB as a 3D matrix (height x width x
251 time) and then time-collapsed to produce a representative two-dimensional image
252 (height x width, I_0 in Figure 1A), where each pixel in I_0 is represented by the maximum
253 intensity value of that pixel across the entire image sequence with its mean value
254 removed. This time-collapsed image I_0 is then used for the rest of the algorithm. Pixels
255 with low intensity values would correspond to static background, whereas pixels with
256 high intensity values would correspond to neurons with GCaMP6 expression. In general,
257 neurons with GCaMP6 expression appear in I_0 as a cluster of adjacent pixels with high
258 intensity values and with size similar to that of a neuron. Meanwhile, it is improbable for

259 random background noise to generate clusters with similar properties. Thus, the time-
260 collapsed image I_0 is expected to contain sufficient information to separate neurons
261 from the background.

262 Next, ACSAT iteratively generates ROIs $\{ROIs\}_n$ from the time-collapsed image I_n for
263 iterations $n = 1, 2, \dots$, starting with $I_1 = I_0$. Prior to each subsequent iteration, I_n is
264 generated by cumulatively clearing previously segmented ROIs, $\{ROIs\}_{n-1}$, from I_{n-1} by
265 setting each ROI's pixels in I_{n-1} to blank values of 0 and dilating the cleared area. As
266 described later, each iteration consists of both adaptive thresholding at the global level
267 (Global FIBAT in Figure 1A), using the automatically selected threshold value τ_n^* (Figure
268 1B), and adaptive thresholding at the local level (Local FIBAT in Figure 1A). When the
269 change in global threshold value $|\tau_{n+1}^* - \tau_n^*|$ is insignificant, further iterations are likely to
270 contribute more false positives than true positives. Thus, the ACSAT algorithm
271 terminates at iteration n if $\frac{|\tau_{n+1}^* - \tau_n^*|}{\tau_1^*} < \delta$ where τ_1^* acts as a normalizing factor.

272 Accordingly, the final output of ACSAT is the union of the segmented ROIs from each
273 iteration, $\{ROIs\}_1 \cup \dots \cup \{ROIs\}_n$.

274 Global and Local Adaptive Thresholding in ACSAT

275 Each iteration n of ACSAT contributes a set of newly segmented ROIs $\{ROIs\}_n$ from I_n
276 by applying our Fluorescence Intensity Based Adaptive Thresholding (FIBAT) algorithm,
277 at the global and local levels (Global/Local FIBAT in Figure 1A). Briefly, FIBAT (Figure
278 1B) takes an inputted image I and outputs the optimal threshold value τ^* which results
279 in optimally segmented ROIs $\{ROIs|\tau^*\}$.

280 Global adaptive thresholding is the first step in the n th iteration of ACSAT (Figure 1A).

281 This step applies FIBAT directly to the whole image ($I_n \rightarrow I$) to identify potential ROIs

282 ($\{ROIs|\tau^*\} \rightarrow \{ROIs\}'_n$).

283 These potential ROIs $\{ROIs\}'_n$ may include groups of adjacent neurons or overlapping

284 neurons because neurons located above and below the focal plane could be captured in

285 the same frame during wide-field imaging. Such overlap however is unlikely to occur in

286 two-photon datasets or in cell culture datasets. The local adaptive thresholding step

287 (Figure 1C) recursively separates any potentially overlapping ROIs within $\{ROIs\}'_n$ in

288 order to output $\{ROIs\}_n$. Specifically, each ROI in $\{ROIs\}'_n$ is individually dilated and then

289 inputted to the local FIBAT ($ROI \rightarrow I$) in (Figure 1B) to obtain a set of separated ROIs

290 $\{ROIs|\tau^*\}$. If any outputted set $\{ROIs|\tau^*\}$ contains more than one separated ROIs, then

291 each ROI in the set $\{ROIs|\tau^*\}$ is further separated using the same procedure, thus

292 forming a recursive loop. Otherwise, if any outputted set $\{ROIs|\tau^*\}$ contains only one

293 ROI, then the recursion terminates. The final output of the local thresholding step

294 $\{ROIs\}_n$ is the union of all such sets containing one ROI that cannot be further

295 separated.

296 Fluorescence Intensity Based Adaptive Thresholding (FIBAT)

297 As described, FIBAT (Figure 1B) is used in both the global and local adaptive

298 thresholding steps of each iteration of ACSAT to identify potential ROIs in the time-

299 collapsed image $I = I_n$ or to separate potentially overlapping neurons within I which is

300 an element of $\{ROIs\}'_n$, respectively. In either case, an optimal pixel intensity threshold

301 value τ^* separates ROIs from the background. FIBAT selects τ^* by searching for the

302 threshold value that maximizes the number of resulting ROIs that are larger in area than
303 A_{min} and smaller in area than A_{max} .

304 The search is performed recursively over a pixel intensity range (τ_1, τ_T) , where initially
305 τ_1 is the minimum pixel intensity value in I and τ_T is the maximum pixel intensity value
306 in I . From this search range, T test threshold values $\tau_1, \tau_2, \dots, \tau_{T-1}, \tau_T$ are uniformly
307 selected. A larger T will decrease the probability of skipping the optimal threshold value,
308 but it will result in more computation time that may not be necessary. Because the
309 threshold value is refined by a recursive process until it reaches the optimal value that
310 produces the maximum number of ROIs, the value of T should have little to no effect on
311 ACSAT's segmentation results. We chose $T = 12$. Each of these test threshold values
312 τ_1, \dots, τ_T is applied to the image I by assigning each pixel a 1 (a true calcium event) if its
313 value is greater than the threshold or a 0 (a false calcium event) otherwise.

314 Morphological operations are then performed to refine the thresholded images.
315 Specifically, these operations fill in holes (0s surrounded by 1s) and remove spur pixels
316 which may be due to noise. The operations also break H-connected ROIs prior to
317 splitting overlapping cells. ROIs are finally collected with 8-connectivity (MATLAB
318 function `bwlabel` or `bwconncomp`) to generate a set of segmented ROIs for each test
319 threshold value: $\{ROIs|\tau_1\}, \dots, \{ROIs|\tau_T\}$.

320 Since ROIs represent real neurons that are roughly spherical in shape and are about 5
321 μm - 20 μm in diameter, some realistic criteria can be used to eliminate false ROIs that
322 are not possibly actual neurons. Accordingly, FIBAT removes ROIs from
323 $\{ROIs|\tau_1\}, \dots, \{ROIs|\tau_T\}$ if their centroid is outside the ROI, or if their area is less than

324 A_{min} or greater than A_{max} , or if their solidity (i.e. the area ratio between the convex hull
 325 of a ROI and the ROI itself) is greater than approximately the golden ratio.

326 The next search range is selected based on the results of the test thresholds. A
 327 relationship of the test threshold values τ_1, \dots, τ_T vs the numbers of resulting ROIs
 328 $|\{ROIs|\tau_1\}|, \dots, |\{ROIs|\tau_T\}|$ can be generated (Figure 1B). If the test threshold value τ_c
 329 resulted in the most ROIs i.e. $c = \arg \max_c |\{ROIs|\tau_c\}|$, then the next search range is set
 330 to $(\tau_{\max\{1, c-1\}}, \tau_{\min\{T, c+1\}})$ in order to include τ_c inside the search range. If more than one
 331 test threshold value $\tau_{c_1}, \tau_{c_2}, \dots$ resulted in the same maximum number of ROIs, then the
 332 next search range is similarly set to $(\tau_{\max\{1, \min\{c_1, c_2, \dots\}-1\}}, \tau_{\min\{T, \max\{c_1, c_2, \dots\}+1\}})$ in order to
 333 contain all $\tau_{c_1}, \tau_{c_2}, \dots$. This search is terminated when further refinement of the search
 334 range produces little improvement in the number of detected ROIs: either the new
 335 search range $|\tau_{c+1} - \tau_{c-1}|$ is less than ϵ or the new range overlaps the previous range
 336 by at least α . We chose $\alpha = 90\%$ and $\epsilon =$ the smallest non-zero intensity difference
 337 between every pair of adjacent pixels in whole image I . As such, ϵ is determined
 338 automatically and does not require user input. Upon termination, the optimal threshold
 339 value is set to $\tau^* = \frac{1}{2}(\min\{\tau_{c_1}, \tau_{c_2}, \dots\} + \max\{\tau_{c_1}, \tau_{c_2}, \dots\})$, and the segmented ROIs
 340 $\{ROIs|\tau^*\}$ includes ROIs whose area exceeds A_{max} .

341 Code accessibility

342 The code/software described in the paper is freely available online at [redacted for
 343 double-blind review]. The code is available in Extended Data 1.

344

345 **Results**

346 We tested ACSAT on 500 simulated datasets, two wide-field hippocampus datasets, a
347 wide-field striatum dataset, a wide-field cell culture dataset, and a two-photon
348 hippocampus dataset. The simulated datasets with known ground truth allowed us to
349 accurately assess the segmentation performance of ACSAT in different conditions of
350 SNR and number of ROIs. For the hippocampus dataset A and the striatum dataset, in
351 which the ground truth is unknown, we used human-generated ROIs as a reference. For
352 the cell culture dataset, hippocampus dataset B, and two-photon dataset, we provide
353 the ACSAT segmented ROIs that can be inspected and interpreted by users.

354 ACSAT performance on simulated datasets with various SNRs and numbers of ROIs

355 To evaluate the performance of ACSAT, we simulated 500 time-collapsed images I_0
356 with various numbers of ROIs (between 300 and 700) at random locations and different
357 SNRs (between ~19 dB and ~29 dB). The exact locations of ROIs are known and
358 served as the ground truth to provide an accurate evaluation of the performance of
359 ACSAT. For all 500 datasets, we used the parameters $\delta = 10\%$, $A_{min} = 50px \approx 86\mu m^2$
360 and $A_{max} = 300px \approx 516\mu m^2$ for the global adaptive thresholding step, and $A_{min} =$
361 $20px \approx 34\mu m^2$ and $A_{max} = \infty$ for the local adaptive thresholding step because ROIs
362 tend to shrink in size after repeatedly applying FIBAT.

363 The recall and precision results for each of these simulated datasets are shown as dots
364 in Figure 2A1 and Figure 2A2, respectively. Figure 2B shows examples of the simulated
365 time-collapsed images, and each example corresponds to a dot in Figure 2A1 and
366 Figure 2A2. At SNR greater than approximately 24 dB, ACSAT shows a stable
367 performance with generally higher than 80% recall. The precision rate remains stable at

368 generally higher than 80% when SNR is greater than approximately 21 dB. However,
369 the performance of ACSAT falls when SNR is below approximately 20 dB.

370 ACSAT performance on hippocampus dataset A and striatum dataset

371 We used ACSAT (Figure 1A) to automatically segment ROIs from a hippocampus wide-
372 field imaging dataset and a striatum wide-field imaging dataset. Prior to the application
373 of the ACSAT, the image sequences were time-collapsed as shown in Figure 3 and
374 Figure 4 (top rows) for the hippocampus A and the striatum datasets, respectively.
375 These time-collapsed images show high intensity areas resembling neural morphology.
376 The final segmented ROIs outputted by ACSAT are illustrated in Figure 3 and Figure 4
377 (bottom row), respectively.

378 For both datasets, we initiated ACSAT using the same parameters as for the simulated
379 datasets ($\delta = 10\%$, $A_{min} = 50px \approx 86\mu m^2$ and $A_{max} = 300px \approx 516\mu m^2$ for the global
380 adaptive thresholding step, and $A_{min} = 20px \approx 34\mu m^2$ and $A_{max} = \infty$ for the local
381 adaptive thresholding step). To obtain the results as shown in Figure 3 and Figure 4, it
382 took approximately one minute per iteration on a Xeon E5-1650 v4 at 3.6GHz with 128
383 GB DDR4 RAM, but it used less than 30 MB RAM. As such, the RAM size had little
384 effect on the speed.

385 ACSAT Performance Compared to Human-Generated ROIs

386 To assess the performance of the ACSAT algorithm, we compared the ACSAT
387 segmentation results with ROIs generated by human inspection (human-generated
388 ROIs). This set of human-generated ROIs contained 423 ROIs for the hippocampus
389 dataset A and 91 ROIs for the striatum dataset. We first compared the ACSAT-

390 generated ROIs for the hippocampus A and striatum datasets with the ROIs in the
391 human-generated ROIs. We consider a pair of ROIs to correspond to the same neuron
392 if they had centroids that were less than $50px \approx 65.6\mu m$ apart and had a mutual overlap
393 greater than 60%. We calculated the mutual overlap as the average of the percentages
394 of the overlapping area against the areas of both ROIs. When there were multiple ROIs
395 sharing overlapping areas, we selected the pair with highest mutual overlap as the
396 matched ROIs.

397 For the hippocampus dataset A, ACSAT identified 445 ROIs after three iterations.
398 Among these 445 ROIs, 317 ROIs were matched in the human-generated ROIs
399 (Match), and 128 ROIs were not in the human-generated ROIs (ACSAT-only).
400 Additionally, 106 ROIs in human-generated ROIs were not identified by ACSAT
401 (Human-only). This result gave us a precision rate of 71.2% (317 out of 445) and a
402 recall rate of 74.9% (317 out of 423). For the striatum dataset, ACSAT was terminated
403 after one iteration and identified a total of 135 ROIs: 69 Match ROIs, 66 ACSAT-only
404 ROIs, and 22 Human-only ROIs (precision rate: 51.1%, recall rate: 75.8%).

405 We further examined the fluorescence traces of ROIs from the ACSAT-only, Human-
406 only, and Match groups. Representative traces are shown in Figure 5A1 and B1,
407 respectively for the hippocampus A and striatum datasets, and all traces are available in
408 Extended Data 2. The value of each ROI fluorescence trace at each timepoint is the
409 average intensity value of all pixels belonging to that ROI. In Figure 5A1 and B1, each
410 trace is normalized by subtracting the mean value of that trace over time and then
411 dividing this difference by that mean value. We calculated the signal-to-noise ratio

412 (SNR) for every ROI in each group. In both the hippocampus A and striatum datasets,
413 the Match ROIs exhibit a broad range of SNR, indicating that both ACSAT and humans
414 are capable of identifying ROIs with various intensities in the time-collapsed image
415 (Figure 5A2 and B2).

416 We further examined the individual ROIs identified by ACSAT that were not identified by
417 humans. This secondary manual inspection found that some of the ACSAT-only ROIs
418 were actually true neurons (i.e. with fluorescence traces compatible with neuronal
419 dynamics) that were missed in the initial human-generated ROIs due to human error.
420 This means that ACSAT was able to segment ROIs that were difficult to identify by
421 human experts. Specifically, for the hippocampus A dataset, 70 (54.7%) out of 128
422 ROIs initially labeled as ACSAT-only were later determined to be actual neurons, and
423 for the striatum dataset, 31 (47%) ROIs were true neurons. After correction, of the total
424 445 ACSAT ROIs from the hippocampus dataset A, 387 segmented ROIs corresponded
425 to true neurons (Match), and 58 segmented ROIs did not correspond to true neurons
426 determined by human inspection (ACSAT-only). Additionally, 106 true ROIs were not
427 segmented (Human-only). This corresponds to a precision rate of 87% and a recall rate
428 of 78.5%. Similarly, for the striatum dataset, which resulted in 135 ACSAT ROIs, there
429 were 100 Match ROIs, 35 ACSAT-only ROIs, and 22 Human-only ROIs after correction.
430 This corresponds to a precision rate of 74.1% and a recall rate of 82%. Even though
431 neurons in the hippocampus and striatum have different morphology and fluorescence
432 intensity, ACSAT was consistently effective for both datasets, and it was able to detect
433 low-intensity neurons that were initially undetected by human referees. As such, our
434 results demonstrate the robustness and effectiveness of the algorithm.

435 The result from the hippocampus dataset A shows that ACSAT successfully identified
436 true ROIs of diverse sizes (Figure 6, red). In general, the false positive ROIs had
437 relatively smaller areas (Figure 6, yellow), similar to the ROIs missed by human
438 referees (Figure 6, green). This indicates that ACSAT is more likely to recognize
439 intensity changes in small areas thereby outperforming human referees under such
440 challenging detection conditions. Additionally, ACSAT missed a small portion of true
441 ROIs, which shares similar sizes with those identified (Figure 6, blue).

442 *Number of Iterations in Using ACSAT*

443 For the hippocampus dataset A, ACSAT was terminated at iteration $n = 3$ when the
444 change in global threshold value $\frac{|\tau_4^* - \tau_3^*|}{\tau_1^*} = 5.12\% < \delta = 10\%$. For the striatum dataset,
445 ACSAT was terminated at iteration $n = 1$ when the change in global threshold value
446 $\frac{|\tau_2^* - \tau_1^*|}{\tau_1^*} = 4.53\% < \delta = 10\%$.

447 To evaluate how ACSAT performs when terminated at different iteration numbers, we
448 ran ACSAT up to 9 iterations on both datasets, and calculated several major
449 performance indicators after each iteration (Figure 7): cumulative number of ROIs,
450 global threshold value, recall, false negative rate, and false discovery rate (which is
451 equal to $1 - \text{precision}$) compared to the human-generated ROIs prior to secondary
452 manual inspection of false positives. The cumulative number of ROIs, recall, and false
453 discovery rate increased with the iteration number, but at different speed. While the
454 cumulative number of ROIs and the false discovery rate increased steadily, recall rose
455 steeply and reached its plateau within approximately three iterations for the
456 hippocampus dataset and after the first iteration for the striatum dataset. Both the global

457 threshold value and the false negative rate dropped as iterations progressed, indicating
458 ACSAT dynamically adjusted the threshold to capture potential ROIs with lower intensity
459 in later iterations. This dynamic adjustment of the threshold value at each iteration was
460 only possible because of the removal of segmented ROIs prior to each iteration.
461 Overall, the changes in these performance indicators over iterations suggested that
462 most true ROIs were identified during the early iterations: $n \leq 3$ for the hippocampus
463 dataset and $n = 1$ for the striatum dataset, which are consistent with when the ACSAT
464 termination criterion described by δ was met. ROIs segmented during later iterations
465 were mostly false positive.

466 FIBAT Global and Local Thresholding

467 In Figure 8, we demonstrate how FIBAT (Figure 1B) determines the threshold value that
468 achieves optimal segmentation results by sampling the distribution of threshold values
469 vs the number of ROIs. Each trace of Figure 8 plots the number of ROIs that results
470 from each sampled threshold value in the global thresholding step during the first four
471 iterations of ACSAT (Figure 1A) on the hippocampus dataset. In each iteration, FIBAT
472 (Figure 1B) first samples the threshold values across the entire intensity range at coarse
473 resolution to identify the potential search range that may result in the maximum number
474 of ROIs. FIBAT further re-samples threshold values within the new search range with a
475 finer resolution, until it reaches a threshold value that gives the maximum number of
476 ROIs. This design allows FIBAT to determine the optimal threshold value with a fine
477 resolution without actually sampling the whole intensity range at the fine scale, and, as
478 a result, reduces the processing time.

479 After performing global thresholding to identify potential ROIs $\{ROIs\}'_n$ (Figure 1A),
480 ACSAT further applies FIBAT locally to each identified ROI in $\{ROIs\}'_n$ to refine the
481 segmentation results (Figure 9). When neurons are densely labeled with GCaMP6,
482 using the global thresholding step alone may lead to one or more large clusters of
483 adjacent neurons being segmented as a single ROI (Figure 9A). For each such cluster,
484 FIBAT (Figure 1B) determines and applies a new threshold value to the local ROI area.
485 With local thresholding, the example cluster is further segmented into 5 new ROIs
486 (Figure 9B), which would not otherwise be separated by applying the global threshold.
487 Because further local thresholding produces the same result (Figure 9C), the local
488 thresholding step of ACSAT concludes that these 5 ROIs cannot be further separated,
489 exits the recursive loop, and outputs these ROIs.

490 To evaluate the efficacy of local thresholding, we examined the hippocampus dataset A
491 at each iteration before and after the local thresholding step (Figure 10, left and right
492 bars, respectively). Local thresholding refined the ROIs detected by global thresholding
493 and captured more true ROIs at every iteration. It is also worth noting that, at later
494 iterations, local thresholding was still able to identify true ROIs that were missed by
495 global thresholding alone (Figure 10, iteration 4).

496 ACSAT performance on two-photon dataset

497 We applied ACSAT to the two-photon dataset Neurofinder 03.00 (Figure 11C).
498 Genetically Encoded Calcium Indicators are generally not expressed in the nuclei (Tian
499 et al., 2009), and because of the optical sectioning technique that two-photon imaging
500 provides, in this dataset the nuclei appear dark. Additionally, this dataset had high
501 speckle noise. Thus, the time-collapsed image generated by ACSAT using max minus

502 mean pixel values shows bright nuclei. The truth file provided by Neurofinder contains
503 621 ROIs, most of which are nuclei. Since the features of this dataset are the nuclei,
504 which are smaller, we used the parameters $\delta = 5\%$, $A_{min} = 20px \approx 6.9\mu m^2$ and
505 $A_{max} = 1000px \approx 34.6\mu m^2$ for the global adaptive thresholding step, and $A_{min} =$
506 $20px \approx 6.9\mu m^2$ and $A_{max} = \infty$ for the local adaptive thresholding step.

507 ACSAT identified 571 ROIs. Among these, 442 ROIs were matched with the truth (true
508 positive), and 179 ROIs were not in the truth (false positive). Additionally, 129 ROIs in
509 truth were not identified by ACSAT (false negative). This result gave us a recall rate of
510 71.2% (442 out of 621) and a precision rate of 77.4% (442 out of 571).

511 We further inspected the time-collapsed image I_0 and observed that the right side of the
512 time-collapsed image I_0 had different patterns of texture than the left side. To utilize the
513 new texture information for ROI detection by ACSAT, we extracted the right side of I_0
514 that is rich in texture information to generate I'_0 as input to ACSAT. The I'_0 was
515 generated by change detection between the original image and its Gaussian-filtered
516 counterpart. Thus, ACSAT identified an additional 157 ROIs, of which 95 were true
517 positives, and 62 were false positives. Combining these additional ROIs with the ROIs
518 identified by direct application of ACSAT results in a recall rate of 82.8% (514 out of 621)
519 and a precision rate of 70.6% (514 out of 728).

520 ACSAT performance on cell culture and hippocampus B dataset

521 Finally, we used ACSAT to detect ROIs in the dataset of the primary neuron culture
522 expressing GCaMP6f (Figure 11B). Qualitatively, it appears ACSAT successfully
523 identified the cell bodies of the majority of neurons in early iterations, and neurites in
524 later iterations. We also used ACSAT to detect ROIs in the hippocampus dataset B

525 (Figure 11A). For both datasets, we used the parameters $\delta = 10\%$, $A_{min} = 50px \approx$
526 $86\mu m^2$ and $A_{max} = 300px \approx 516\mu m^2$ for the global adaptive thresholding step, and
527 $A_{min} = 20px \approx 34\mu m^2$ and $A_{max} = \infty$ for the local adaptive thresholding step because
528 ROIs tend to shrink in size after repeatedly applying FIBAT.

529 Discussion

530 In this study, we presented our Automated Cell Segmentation by Adaptive Thresholding
531 (ACSAT) method that adaptively selects threshold values based on image pixel intensity
532 with two iterative steps at the global and local levels using a time-collapsed image. As
533 such, the algorithm is capable of handling morphological variations in fluorescence
534 intensity in neurons and is robust against luminance condition changes across datasets.
535 When applied to two datasets collected from the hippocampus and the striatum in mice,
536 ACSAT resulted in approximately 80% recall rate of regions of interest (ROIs)
537 containing individual neurons (78.5% for the hippocampus A dataset and 82% for the
538 striatum dataset), and approximately 80% precision rate (87% for the hippocampus
539 dataset and 74.1% for the striatum dataset). ACSAT was also able to detect low-
540 intensity ROIs that were initially undetected by human referees. When applied to 500
541 simulated datasets, ACSAT achieved recall and precision rates higher than 80% when
542 SNR was no less than approximately 24 dB. However, the performance of ACSAT falls
543 when SNR reaches below approximately 20 dB.

544 The ACSAT algorithm is an intuitive thresholding method that uses global and local
545 schemes to address variations in fluorescence intensity levels of GCaMP6 fluorescence
546 even within the same image field. Simply applying a lower global threshold value would
547 result in few large ROIs containing multiple neurons within one ROI. On the other hand,

548 with a high global threshold value, only a small number of neurons with high intensity
549 would be found. As such, applying a single high or low threshold value would generate
550 inadequate results of either few or excessive ROIs, which is a universal limitation of
551 thresholding methods. Our algorithm efficiently addresses this challenge in two ways.

552 First, it cumulatively excludes previously segmented ROIs from the time-collapsed
553 image I_n after each iteration so that in the following iteration, ACSAT could detect new
554 ROIs that require distinct thresholds to separate but were missed with previous
555 thresholds. Therefore, the global threshold value τ_n^* (Figure 1) used by ACSAT usually
556 decreases after each iteration, and ROIs with high intensity were segmented before
557 those with low intensity, as shown in Figure 3 and Figure 4. Because ACSAT is based
558 on adaptive thresholding, it allows us to objectively and robustly segment ROIs with low
559 intensity relative to the background. These low-intensity areas often pose challenges to
560 human experts when manually detecting ROIs, as our results showed that about half of
561 the ROIs initially labeled as false positive were actually true neurons (Figure 10).

562 Second, ACSAT uses Fluorescence Intensity Based Adaptive Thresholding (FIBAT)
563 locally to separate overlapping ROIs. This approach directly addresses the issue of
564 heterogeneity in recorded neural signals when the intensities of pixels surrounding an
565 ROI can vary. However, because a higher thresholding value is usually required to
566 separate adjoining neurons, the output sub-ROIs after local FIBAT are often smaller
567 than the corresponding true neurons. Thus, a simple dilation step was applied during
568 the local FIBAT step. This correction is useful to prevent real ROIs from falling below
569 the minimum area criteria A_{min} and thus being removed. Although the interleaving
570 process of global FIBAT and local FIBAT has been effective in addressing overlapping

571 neurons, a potential problem still arises if two neurons with similar intensities have
572 significant overlap with each other in the time-collapsed image such that there is no
573 trough between them. Then ACSAT may identify them as a single ROI. Conversely, if
574 there is a neuron with multiple hot-spots (Pnevmatikakis et al., 2016), then this may be
575 identified as multiple neurons by ACSAT. Such a scenario, however, can be minimized
576 by the minimum area criteria A_{min} and the maximum area criteria A_{max} . Spatial overlap
577 is profound for wide-field imaging, but not for two-photon imaging or in vitro cell culture
578 imaging with single cell layer. With increasing improvement wide-field imaging, such as
579 volumetric imaging (Shain et al., 2018, Xiao et al., 2018), such significant overlap may
580 be better eliminated during data acquisition step.

581 ACSAT has three sets of free parameters that can be rationally chosen or otherwise are
582 not sensitive: δ which describes the termination condition for ACSAT, α which describes
583 a termination condition for FIBAT, and A_{min} and A_{max} which describe the allowed sizes
584 of ROIs.

585 The termination condition for ACSAT, described by δ , can be explained by the
586 tendencies of ACSAT. Specifically, running ACSAT for more iterations increases the
587 number of ROIs segmented, especially the number of low-intensity ROIs, as the global
588 threshold value τ_n^* gradually decreases (Figure 7). While many of the added ROIs are
589 true ROIs, the proportion of false positive ROIs added increases as iteration number
590 increases (Figure 7). This increasing proportion of outputted false positives in later
591 iterations can be attributed to the higher probability of a spurious collection of adjacent
592 background pixels meeting the criteria to be an ROI. Also, the added false positives can
593 be related to the step which clears previously segmented ROIs from the time-collapsed

594 image at the start of each iteration of ACSAT. Due to the scattering of light in brain
595 tissue, ROI removal may leave a few small fragments of bright pixels around removed
596 areas, which could be identified as ROIs during the next iteration. ACSAT tries to avoid
597 this problem by dilating the cleared area which makes sure the whole ROI is cleared
598 rather than only the brighter center. Besides dilation, these misidentified ROIs were also
599 discarded either because of their small size or because they do not meet the solidity
600 criteria; however, occasionally they may pass the size criteria and become the false
601 positive ROIs. As a result, the majority of false positives tend to have small size (Figure
602 6, yellow).

603 In order to balance the effects of simultaneous increase in true ROIs and false positive
604 ROIs, ACSAT stops when a decrease of global threshold value becomes relatively
605 small between iterations i.e. $\frac{|\tau_{n+1}^* - \tau_n^*|}{\tau_1^*} < \delta$. At that stage, most true ROIs have been
606 detected and removed from the time-collapsed image. Thus, the global threshold values
607 τ_n^* of any further iterations are similar, so most ROIs detected at this stage are false
608 positives. For the hippocampus dataset A, iteration $n = 3$ is when the increase in false
609 positives begins to outweigh the increase in true positives, and for the striatum dataset,
610 nearly all true ROIs segmented by ACSAT were outputted at iteration $n = 1$ (Figure 7).
611 Qualitatively, the time-collapsed image I_0 for hippocampus has a higher density of
612 neurons with a greater variety of pixel intensities than the I_0 for striatum, so it may take
613 more iterations for ACSAT to perform at the same rate on the hippocampus dataset
614 than on the striatum dataset. ACSAT's performance under the diverse conditions of
615 these two datasets suggests that our choice of $\delta = 10\%$ provides a robust and rational
616 termination condition for ACSAT that can be generalized to other datasets, namely the

617 500 simulated datasets and the cell culture dataset, as well. In fact, changing the
618 termination condition from $\delta = 10\%$ to $\delta = 5\%$ only affected the segmentation results in
619 less than 17% of the 500 simulated datasets. For the two-photon dataset, our reported
620 results are using the termination condition $\delta = 5\%$. In general, users can choose δ to be
621 between 5% and 10% based on the needs of their application: if recall is more important,
622 then users should choose a smaller δ , and if precision is more important, then users
623 should choose a larger δ .

624 Additionally, the final segmentation results generated by ACSAT are not sensitive to the
625 termination conditions for FIBAT described by α and ϵ . FIBAT is terminated if the
626 threshold search range has minimal change over an iteration, which we determine in
627 two ways. One way this condition would be satisfied is when all threshold values within
628 the search range result in the same, optimal number of ROIs. This is equivalent to
629 setting the criteria $\alpha = 100\%$. For the practical purpose of reducing FIBAT run time, we
630 allow termination if the change in the search range is less than $1 - \alpha = 10\%$. This
631 condition is also easily met when FIBAT is used in the local thresholding step because,
632 by definition, ROIs that cannot be separated by FIBAT will return exactly one ROI no
633 matter what threshold value is used. Additionally, we terminate FIBAT if the search
634 range is smaller than ϵ , the smallest difference between any pair of adjacent pixels in I ,
635 which can be objectively and automatically determined from I . If FIBAT were to continue
636 refining the threshold value, then the gained precision beyond that defined by ϵ would
637 be useless due to the discrete step in pixel intensity values in I .

638 The last set of parameters A_{min} and A_{max} should be chosen based on how large
639 neurons are expected to be using information including neuron size, image resolution,

640 magnification, imaging method, etc. In our wide-field datasets, the boundaries of
641 neurons may not be as well-defined as those collected with two-photon microscope, and
642 the size will appear larger than the size of a neuron due to light scattering in wide-field
643 conditions. This effect is consistent with our observation that the minimum size of the
644 human-generated ROIs was $38px \approx 64.6\mu m^2$ for the hippocampus A dataset and
645 $66px \approx 112.2\mu m^2$ for the striatum dataset. Thus, our minimum ROI criteria for the wide-
646 field datasets may be larger than a typical neuron size.

647 The images I_0 used by ACSAT are time-collapsed, and therefore do not contain any
648 temporal information. With the flexibility of ACSAT, the framework of ACSAT can be
649 used as long as a single image can be generated to represent the ROIs within the
650 image sequence. For example, an input image I'_0 can be generated where the value of
651 each pixel represents the time of its maximum intensity. This image I'_0 would allow
652 ACSAT to separate adjoined ROIs that have similar intensity values in I_0 but reach their
653 maximum intensity at different time points, which is described by I'_0 . Other ways to
654 generate the single representative image include correlations with nearby pixels,
655 intensity dynamics such as standard deviation or variance over time, texture of the time-
656 collapsed image (for example, as used for the two-photon dataset), and a combination
657 of various parameters. Overall, by taking advantage of adaptively determining the
658 threshold value at both the global level and the local level, ACSAT can theoretically
659 perform segmentation on any image containing ROIs with non-homogenous intensity as
660 long as it has sufficient contrast between ROIs and the background.

661

662 **References**

- 663 Allen WE, Kauvar IV, Chen MZ, Richman EB, Yang SJ, Chan K, Gradinaru V, Deverman BE,
664 Luo L, Deisseroth K (2017) Global Representations of Goal-Directed Behavior in Distinct
665 Cell Types of Mouse Neocortex. *Neuron* 94:891-907 e896.
- 666 Andermann ML, Kerlin AM, Reid RC (2010) Chronic cellular imaging of mouse visual cortex
667 during operant behavior and passive viewing. *Front Cell Neurosci* 4:3.
- 668 Chen TW, Wardill TJ, Sun Y, Pulver SR, Renninger SL, Baohan A, Schreier ER, Kerr RA,
669 Orger MB, Jayaraman V, Looger LL, Svoboda K, Kim DS (2013) Ultrasensitive
670 fluorescent proteins for imaging neuronal activity. *Nature* 499:295-300.
- 671 Dombeck DA, Khabbaz AN, Collman F, Adelman TL, Tank DW (2007) Imaging large-scale
672 neural activity with cellular resolution in awake, mobile mice. *Neuron* 56:43-57.
- 673 Fantuzzo JA, Mirabella VR, Hamod AH, Hart RP, Zahn JD, Pang ZP (2017) Intellicount: High-
674 Throughput Quantification of Fluorescent Synaptic Protein Puncta by Machine Learning.
675 *eNeuro* 4.
- 676 Ghosh KK, Burns LD, Cocker ED, Nimmerjahn A, Ziv Y, Gamal AE, Schnitzer MJ (2011)
677 Miniaturized integration of a fluorescence microscope. *Nat Methods* 8:871-878.
- 678 Hamel EJ, Grewe BF, Parker JG, Schnitzer MJ (2015) Cellular level brain imaging in behaving
679 mammals: an engineering approach. *Neuron* 86:140-159.
- 680 Hofer SB, Ko H, Pichler B, Vogelstein J, Ros H, Zeng H, Lein E, Lesica NA, Mrcic-Flogel TD
681 (2011) Differential connectivity and response dynamics of excitatory and inhibitory
682 neurons in visual cortex. *Nat Neurosci* 14:1045-1052.
- 683 Huber D, Gutnisky DA, Peron S, O'Connor DH, Wiegert JS, Tian L, Oertner TG, Looger LL,
684 Svoboda K (2012) Multiple dynamic representations in the motor cortex during
685 sensorimotor learning. *Nature* 484:473-478.
- 686 Issa JB, Haeffele BD, Agarwal A, Bergles DE, Young ED, Yue DT (2014) Multiscale optical
687 Ca²⁺ imaging of tonal organization in mouse auditory cortex. *Neuron* 83:944-959.
- 688 Kim TH, Zhang Y, Lecoq J, Jung JC, Li J, Zeng H, Niell CM, Schnitzer MJ (2016) Long-Term
689 Optical Access to an Estimated One Million Neurons in the Live Mouse Cortex. *Cell*
690 *reports* 17:3385-3394.
- 691 Lutcke H, Gerhard F, Zenke F, Gerstner W, Helmchen F (2013) Inference of neuronal network
692 spike dynamics and topology from calcium imaging data. *Front Neural Circuits* 7:201.
- 693 Mellen NM, Tuong CM (2009) Semi-automated region of interest generation for the analysis of
694 optically recorded neuronal activity. *Neuroimage* 47:1331-1340.
- 695 Mohammed AI, Gritton HJ, Tseng HA, Bucklin ME, Yao Z, Han X (2016) An integrative
696 approach for analyzing hundreds of neurons in task performing mice using wide-field
697 calcium imaging. *Sci Rep* 6:20986.
- 698 Moyer JR, Jr., Deyo RA, Disterhoft JF (1990) Hippocampectomy disrupts trace eye-blink
699 conditioning in rabbits. *Behav Neurosci* 104:243-252.
- 700 Mukamel EA, Nimmerjahn A, Schnitzer MJ (2009) Automated analysis of cellular signals from
701 large-scale calcium imaging data. *Neuron* 63:747-760.
- 702 Ohki K, Chung S, Ch'ng YH, Kara P, Reid RC (2005) Functional imaging with cellular resolution
703 reveals precise micro-architecture in visual cortex. *Nature* 433:597-603.
- 704 Otsu N (1979) Threshold Selection Method from Gray-Level Histograms. *Ieee T Syst Man Cyb*
705 9:62-66.
- 706 Pinto L, Dan Y (2015) Cell-Type-Specific Activity in Prefrontal Cortex during Goal-Directed
707 Behavior. *Neuron* 87:437-450.
- 708 Pnevmatikakis EA, Soudry D, Gao Y, Machado TA, Merel J, Pfau D, Reardon T, Mu Y,
709 Lacefield C, Yang W, Ahrens M, Bruno R, Jessell TM, Peterka DS, Yuste R, Paninski L
710 (2016) Simultaneous Denoising, Deconvolution, and Demixing of Calcium Imaging Data.
711 *Neuron* 89:285-299.

- 712 Poort J, Khan AG, Pachitariu M, Nemri A, Orsolich I, Krupic J, Bauza M, Sahani M, Keller GB,
713 Mrsic-Flogel TD, Hofer SB (2015) Learning Enhances Sensory and Multiple Non-
714 sensory Representations in Primary Visual Cortex. *Neuron* 86:1478-1490.
- 715 Sadeghian F, Seman Z, Ramli AR, Abdul Kahar BH, Saripan MI (2009) A framework for white
716 blood cell segmentation in microscopic blood images using digital image processing. *Biol*
717 *Proced Online* 11:196-206.
- 718 Sakamoto T, Takatsuki K, Kawahara S, Kirino Y, Niki H, Mishina M (2005) Role of hippocampal
719 NMDA receptors in trace eyeblink conditioning. *Brain Res* 1039:130-136.
- 720 Sezgin M, Sankur B (2004) Survey over image thresholding techniques and quantitative
721 performance evaluation. *J Electron Imaging* 13:146-168.
- 722 Shain WJ, Vickers NA, Li J, Han X, Bifano T, Mertz J (2018) Axial localization with modulated-
723 illumination extended-depth-of-field microscopy. *Biomed Opt Express* 9:1771-1782.
- 724 Shen S, Syal K, Tao N, Wang S (2015) An automated image analysis method for high-
725 throughput classification of surface-bound bacterial cell motions. *Rev Sci Instrum*
726 86:126104.
- 727 Solomon PR, Vander Schaaf ER, Thompson RF, Weisz DJ (1986) Hippocampus and trace
728 conditioning of the rabbit's classically conditioned nictitating membrane response. *Behav*
729 *Neurosci* 100:729-744.
- 730 Sun XR, Badura A, Pacheco DA, Lynch LA, Schneider ER, Taylor MP, Hogue IB, Enquist LW,
731 Murthy M, Wang SS (2013) Fast GCaMPs for improved tracking of neuronal activity. *Nat*
732 *Commun* 4:2170.
- 733 Tian L, Hires SA, Mao T, Huber D, Chiappe ME, Chalasani SH, Petreanu L, Akerboom J,
734 McKinney SA, Schreier ER, Bargmann CI, Jayaraman V, Svoboda K, Looger LL (2009)
735 Imaging neural activity in worms, flies and mice with improved GCaMP calcium
736 indicators. *Nat Methods* 6:875-881.
- 737 Tseng W, Guan R, Disterhoft JF, Weiss C (2004) Trace eyeblink conditioning is hippocampally
738 dependent in mice. *Hippocampus* 14:58-65.
- 739 Wachowiak M, Economo MN, Diaz-Quesada M, Brunert D, Wesson DW, White JA, Rothermel
740 M (2013) Optical dissection of odor information processing in vivo using GCaMPs
741 expressed in specified cell types of the olfactory bulb. *J Neurosci* 33:5285-5300.
- 742 Wilt BA, Fitzgerald JE, Schnitzer MJ (2013) Photon shot noise limits on optical detection of
743 neuronal spikes and estimation of spike timing. *Biophys J* 104:51-62.
- 744 Xiao S, Tseng HA, Gritton H, Han X, Mertz J (2018) Video-rate volumetric neuronal imaging
745 using 3D targeted illumination. *Sci Rep* 8:7921.
- 746 Zhou P, Resendez SL, Rodriguez-Romaguera J, Jimenez JC, Neufeld SQ, Giovannucci A,
747 Friedrich J, Pnevmatikakis EA, Stuber GD, Hen R, Kheirbek MA, Sabatini BL, Kass RE,
748 Paninski L (2018) Efficient and accurate extraction of in vivo calcium signals from
749 microendoscopic video data. *Elife* 7.
- 750 Ziv Y, Burns LD, Cocker ED, Hamel EO, Ghosh KK, Kitch LJ, El Gamal A, Schnitzer MJ (2013)
751 Long-term dynamics of CA1 hippocampal place codes. *Nat Neurosci* 16:264-266.
- 752
- 753

754 **Figure Captions**

755 Figure 1. **Flowchart of the Automated Cell Segmentation by Adaptive**

756 **Thresholding (ACSAT) algorithm.** (A) The input is the time-collapsed image I_0 , and
757 the output is a collection of automatically segmented ROIs. In each iteration, the "Global
758 FIBAT" step identifies potential ROIs $\{ROIs\}'_n$ by applying FIBAT, described in part B, to
759 the entire image I_n ; and the "Local FIBAT" step, described in part C, splits overlapping
760 ROIs. (B) Flowchart of the Fluorescence Intensity Based Adaptive Thresholding (FIBAT)
761 algorithm. The input image is segmented using each of the test threshold values
762 $\tau_1, \tau_2, \dots, \tau_T$. The search range for the optimal threshold value (τ_1, τ_T) is iteratively
763 narrowed to contain the test threshold value which results in the maximum number of
764 ROIs. (C) Local FIBAT procedure. FIBAT, described in part B, is recursively applied to
765 each potential ROI until the resulting ROI(s) can no longer be separated by FIBAT.

766 Figure 2. **ACSAT performance on simulated datasets.** (A1) Recall and (A2) precision
767 are plotted as a function of signal-to-noise ratio (SNR) and number of ROIs. Each dot
768 corresponds to the ACSAT result for one of the 500 simulated datasets. A surface was
769 fitted to these dots for visualization. The black vertical plane corresponds to the SNR of
770 the hippocampus A dataset. (B) Six examples of simulated time-collapsed images,
771 labeled a-f, correspond to the dots labeled a-f in parts A1 and A2.

772 Figure 3. **Hippocampus dataset A and ROIs identified by ACSAT.** (A) The
773 aggregated image of hippocampus dataset A and zoom-in images (Ai, Aii, and Aiii,
774 corresponding to the grey boxes). (B) ACSAT determined ROIs from multiple iterations
775 overlying on the aggregated image (red, yellow, green, and blue outline corresponds to

776 iteration 1, 2, 3, and 4, respectively). The fourth iteration (blue) is shown for comparison
777 although ACSAT terminated at iteration 3 (red, yellow, and green).

778 Figure 4. **Striatum dataset and ROIs identified by ACSAT.** (A) The aggregated image
779 of striatum dataset and zoom-in images (Ai, Aii, and Aiii, corresponding to the grey
780 boxes). (B) ACSAT determined ROIs from multiple iterations overlying on the
781 aggregated image (red, yellow, green, and blue outline corresponds to iteration 1, 2, 3,
782 and 4, respectively). The second (yellow), third (green), and fourth (blue) iterations are
783 shown for comparison although ACSAT terminated at iteration 1 (red).

784 Figure 5. **Fluorescence traces and signal-to-noise ratios.** (A1) Representative
785 fluorescence traces from the hippocampus dataset A for ROIs identified by both ACSAT
786 and human referees (Match). ROIs identified only by ACSAT (ACSAT), and ROIs
787 identified only by human referees (Human). (A2) Histogram of signal-to-noise ratio
788 (SNR) for Match, ACSAT, and Human ROIs from the hippocampus dataset A. (B1)
789 Representative fluorescence traces from the striatum dataset. (B2) Histogram of SNR
790 for the striatum dataset.

791 Figure 6. **Distribution of ROI size.** ACSAT identified true ROIs (red) with various size.
792 The false positive ROIs (yellow) and those missed by human experts (green) tend to
793 have small areas, while the areas of false negative ROIs (blue) appear slightly larger.

794 Figure 7. **Performance of ACSAT over iterations.** For both (A) hippocampus dataset
795 A and (B) striatum dataset, the cumulative number of identified ROIs (blue line)
796 increased steadily over iterations. The global threshold (dash blue line) tended to
797 decrease with each iteration, allowing ACSAT to capture ROIs with lower intensity. Both

798 recall (solid red line) and false discovery rate = $1 - \text{precision}$ (dotted red line) increased
799 with iterations, while the false negative rate (dashed red line) decreased. All results
800 reported here are based on human-generated ROIs prior to secondary manual
801 inspection of false positives.

802 **Figure 8. Convergence of the FIBAT optimal global threshold value for the**
803 **hippocampus dataset A.** FIBAT first sampled at a coarse scale across a wide intensity
804 range, and then focused on a small potential intensity range with a fine scale to identify
805 the optimal global threshold value that generated most ROIs. The vertical lines indicate
806 the final optimal global threshold value determined by FIBAT for each iteration.

807 **Figure 9. Improved ROI identification by local thresholding.** (A) With global
808 thresholding alone, a cluster of hippocampal neurons was identified as a single ROI. (B)
809 After application of local thresholding, ACSAT successfully separated five new ROIs
810 from the single ROI. (C) Zoom-in of each ROI separated by local thresholding.

811 **Figure 10. Local thresholding improves ACSAT performance.** The ROIs identified by
812 ACSAT at each iteration before local thresholding (left) and after (right). Local
813 thresholding separated overlapping ROIs and thus helped identify more ROIs, including
814 those identified by human (black) or missed by human (red).

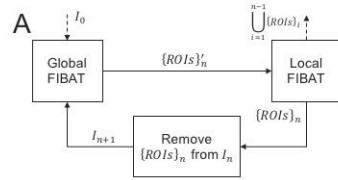
815 **Figure 11. ACSAT results of various datasets.** (A) The time-collapsed image of
816 hippocampus dataset B (top) with ACSAT ROIs overlaid (bottom). (B) The time-
817 collapsed image for the primary neuron culture dataset (top) with ACSAT ROIs overlaid
818 (bottom). (C) The time-collapsed image for the two-photon dataset (Neurofinder 03.00)
819 (top) with ACSAT ROIs overlaid (bottom). For all three datasets, the majority of ROIs

820 were identified during the first two iterations. Red, yellow, green, and blue ROI outline
821 corresponds to iteration 1, 2, 3, and 4, respectively.

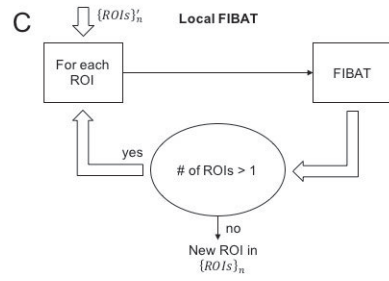
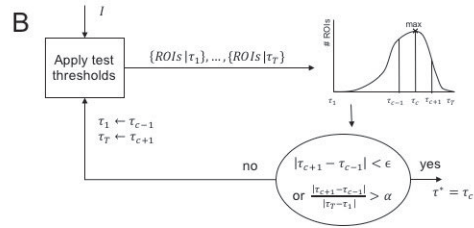
822 Extended Data 1. ZIP file contains eleven MATLAB files which comprise the ACSAT
823 algorithm.

824 Extended Data 2. Fluorescence traces in a MATLAB struct for all ROIs in the
825 hippocampus dataset A and the striatum dataset grouped into “Match,” “ACSAT,” and
826 “Human” as defined in Figure 5. Groupings here are based on human-generated ROIs
827 prior to secondary manual inspection of ACSAT-only ROIs.

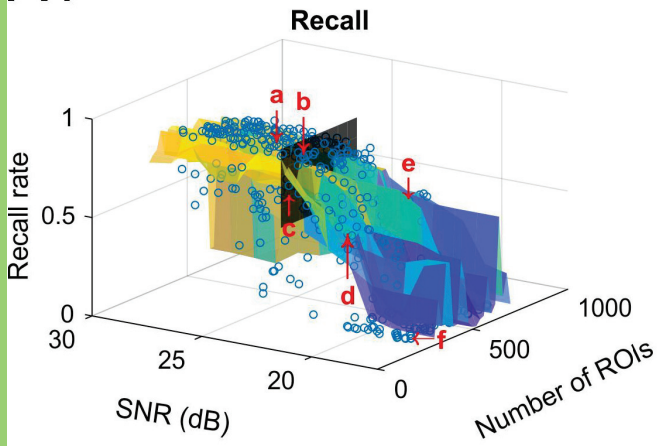
Automated Cell Segmentation by Adaptive Thresholding (ACSAT)



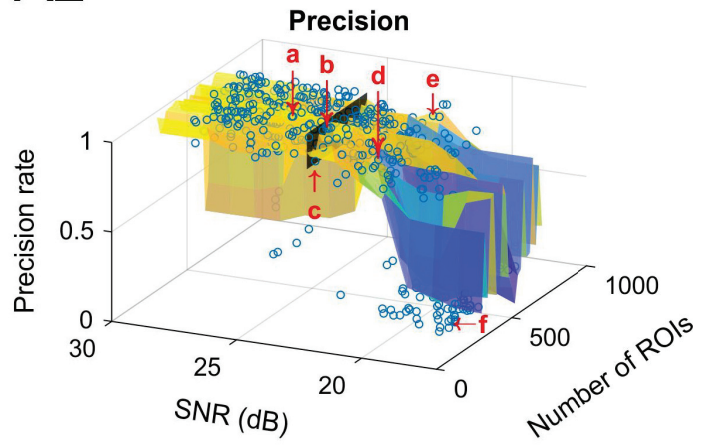
Fluorescence Intensity Based Adaptive Thresholding (FIBAT)



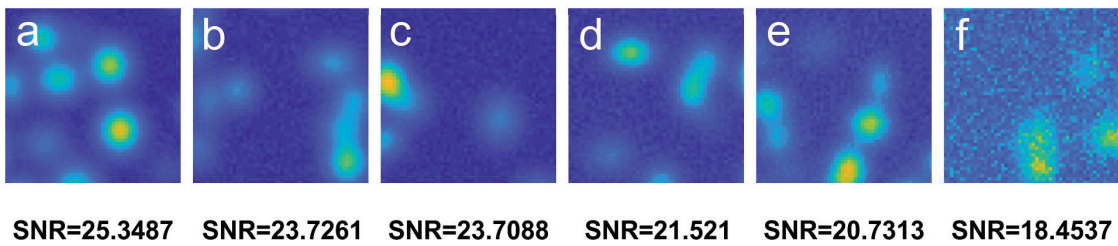
A1

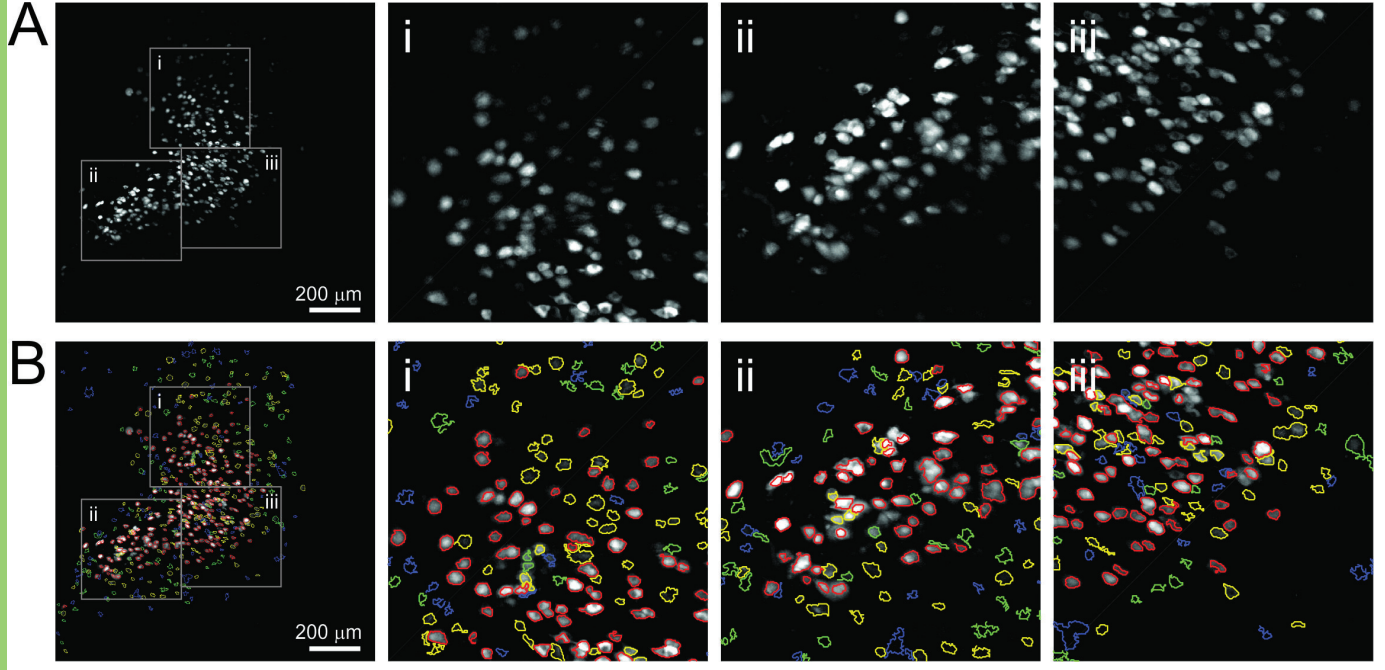


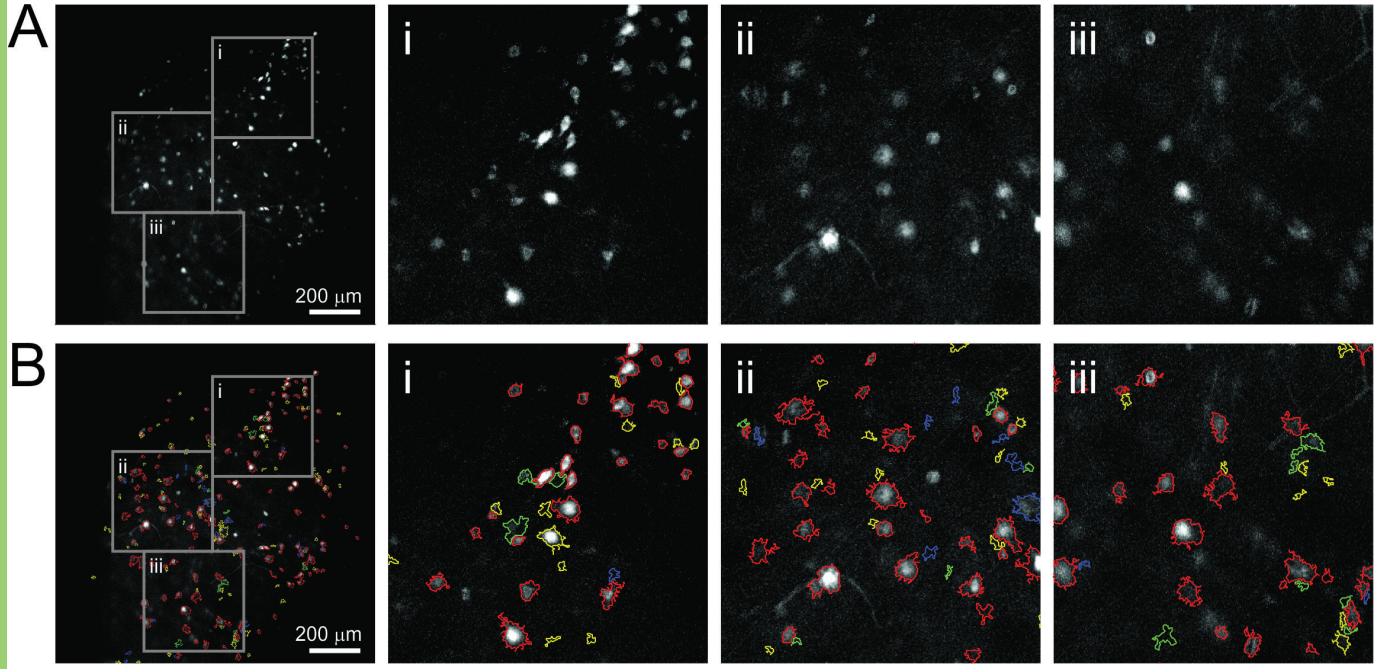
A2



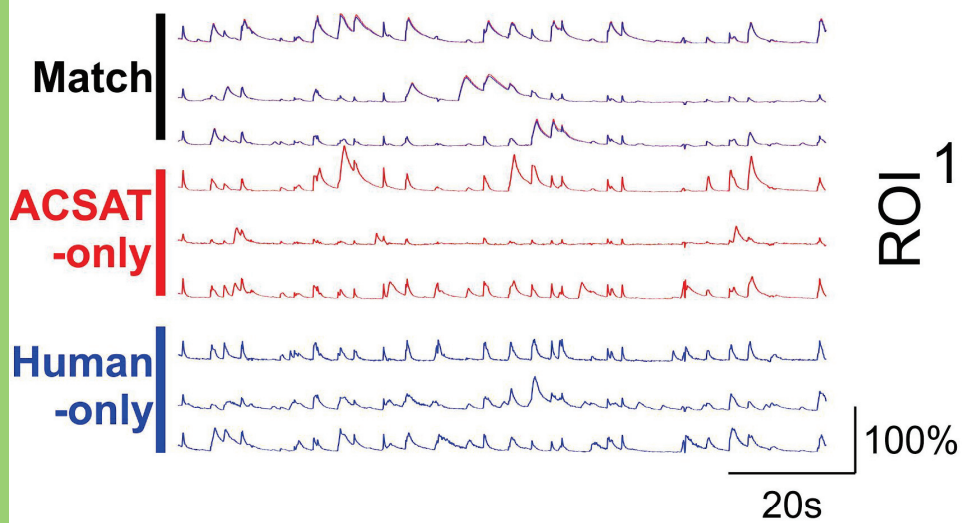
B



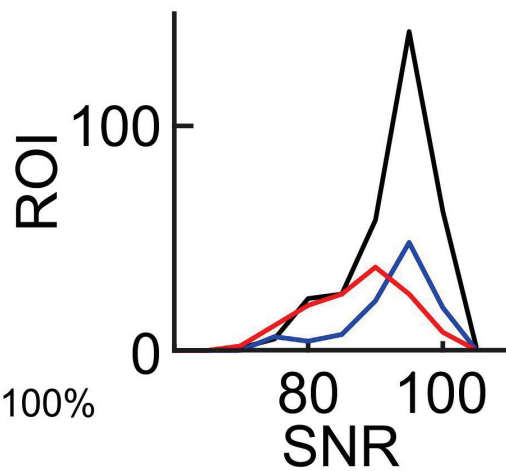




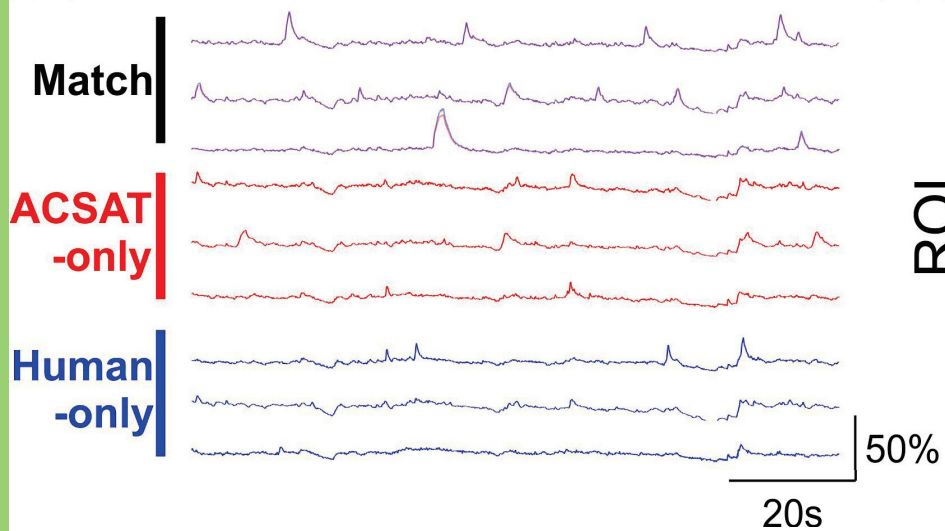
A1



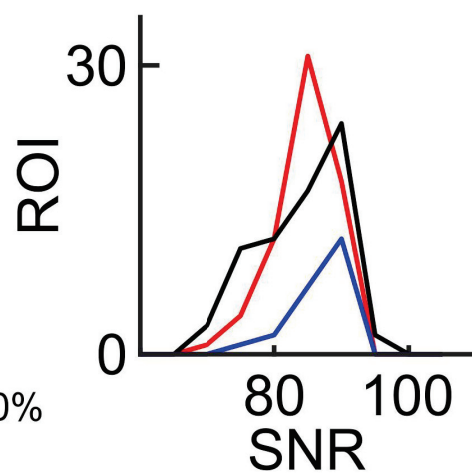
A2

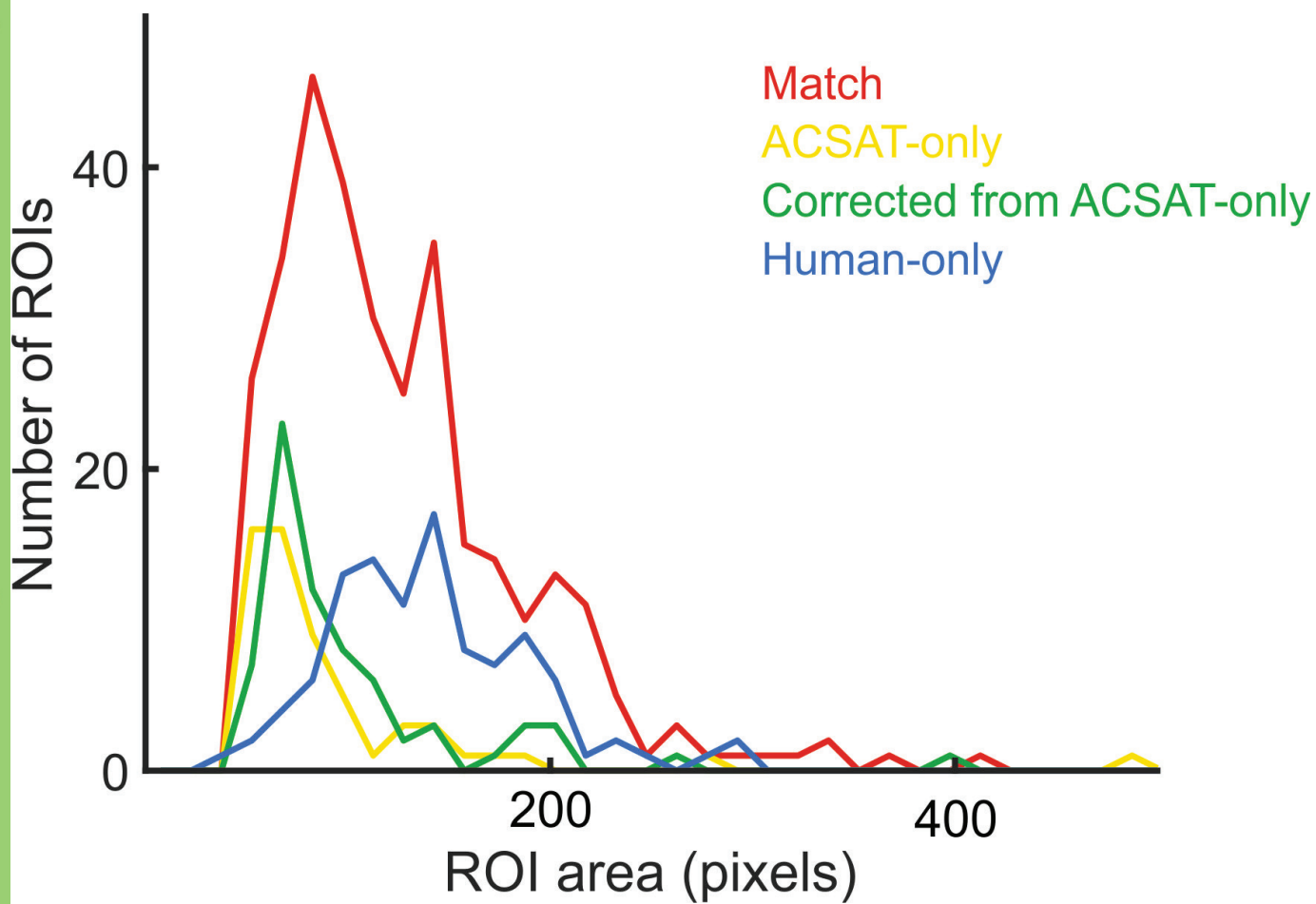


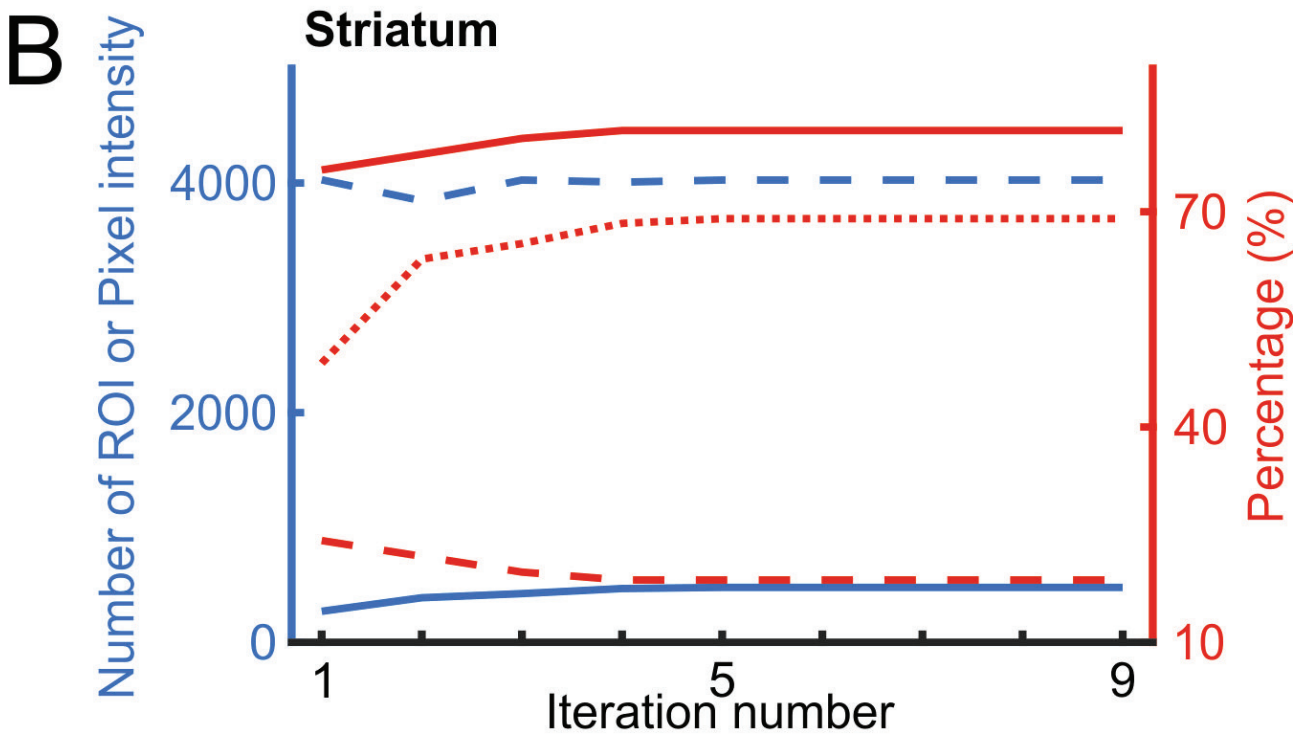
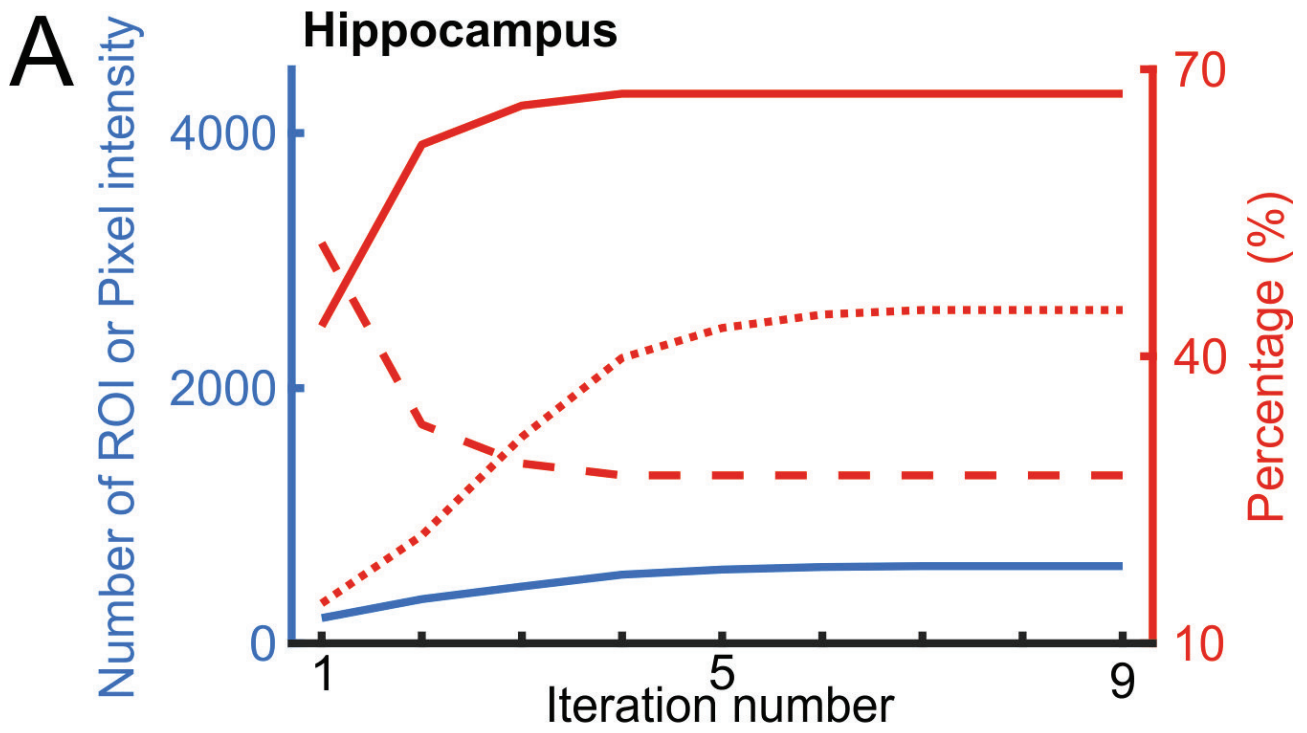
B1



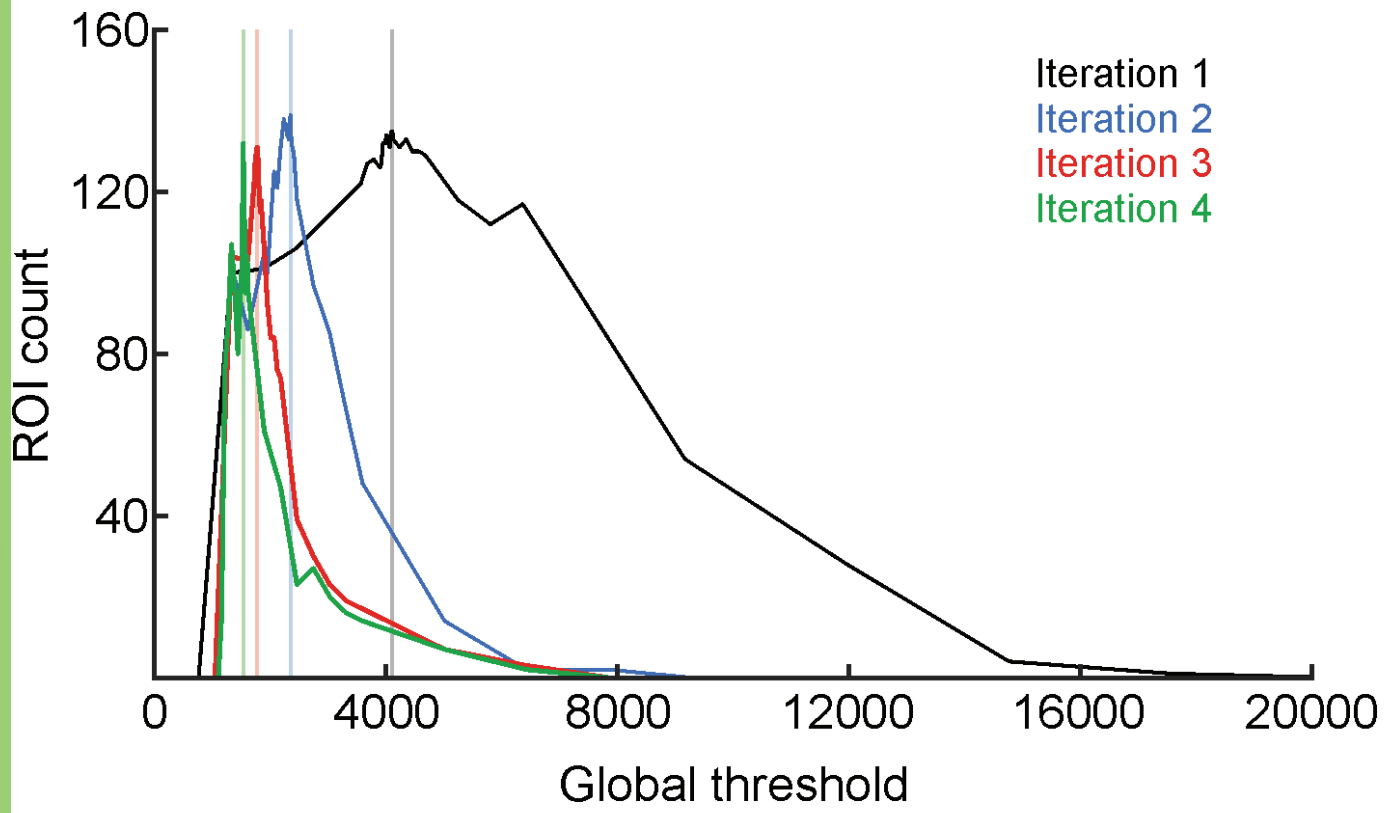
B2

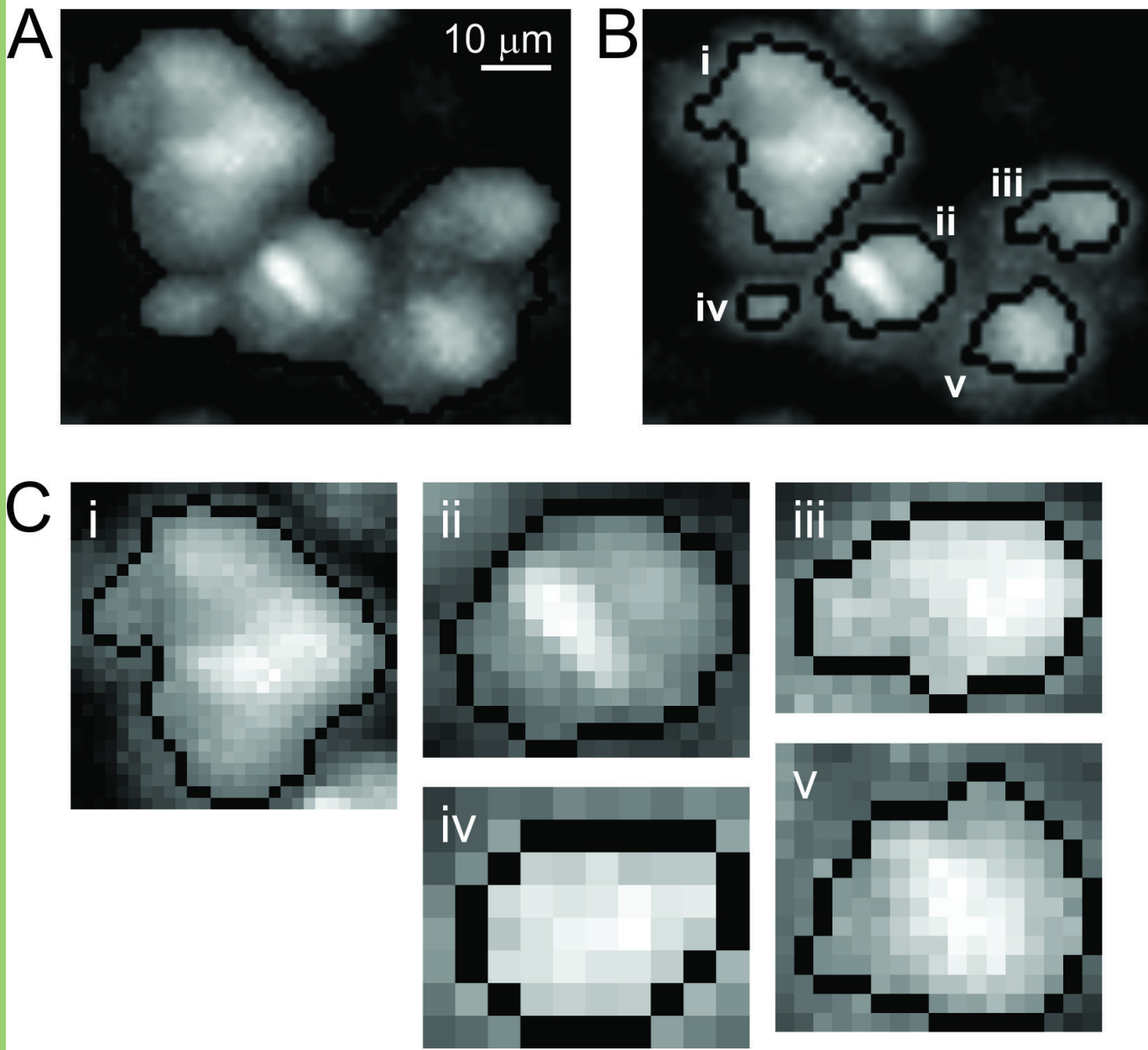


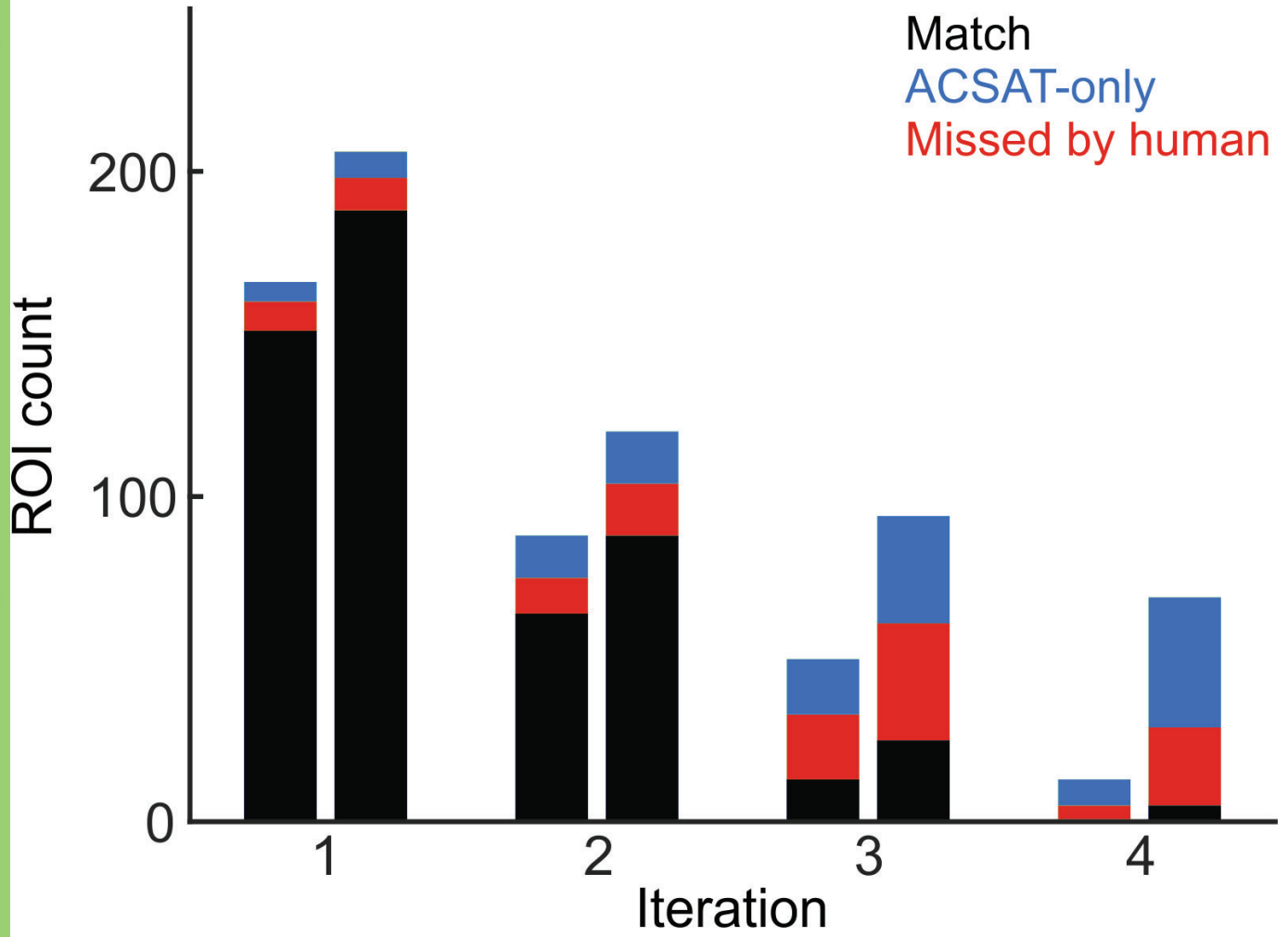




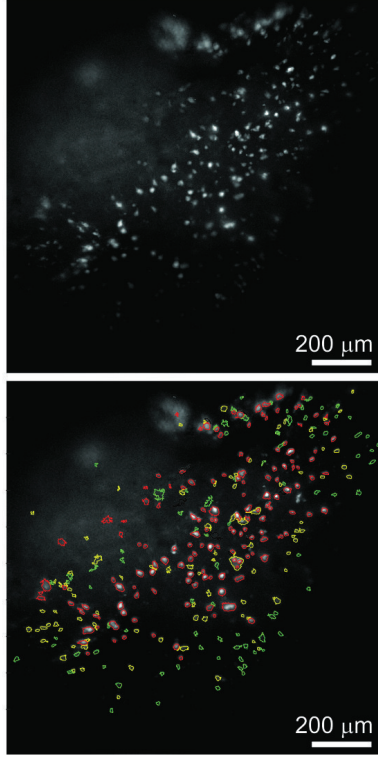
— ROI count — Match
- - Global threshold - - Human-only
..... ACSAT-only



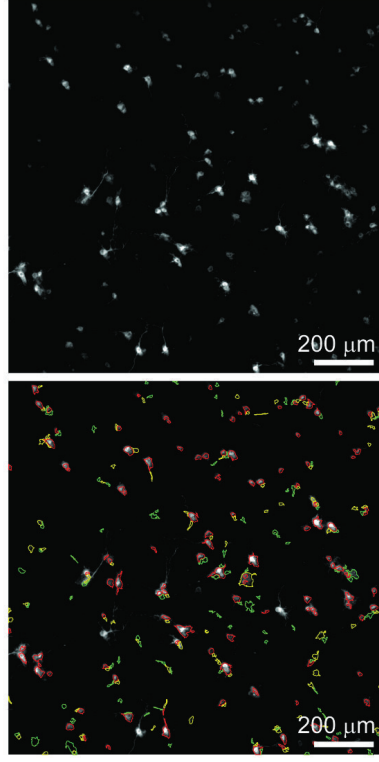




A



B



C

